




Branching Exponents of Synthetic Vascular Trees Under Different Optimality Principles

Etienne Jessen , Marc C. Steinbach , Charlotte Debbaut , and Dominik Schillinger 

Abstract—Objective: The branching behavior of vascular trees is often characterized using Murray’s law. We investigate its validity using synthetic vascular trees generated under global optimization criteria. **Methods:** Our synthetic tree model does not incorporate Murray’s law explicitly. Instead, we show that its validity depends on properties of the optimization model and investigate the effects of different physical constraints and optimization goals on the branching exponent that is now allowed to vary locally. In particular, we include variable blood viscosity due to the Fåhræus–Lindqvist effect and enforce an equal pressure drop between inflow and the micro-circulation. Using our global optimization framework, we generate vascular trees with over one million terminal vessels and compare them against a detailed corrosion cast of the portal venous tree of a human liver. **Results:** Murray’s law is fulfilled when no additional constraints are enforced, indicating its validity in this setting. Variable blood viscosity or equal pressure drop lead to different optima but with the branching exponent inside the experimentally predicted range between 2.0 and 3.0. The validation against the corrosion cast shows good agreement from the portal vein down to the venules. **Conclusion:** Not enforcing Murray’s law increases the predictive capabilities of synthetic vascular trees, and in addition reduces the computational cost. **Significance:** The ability to study optimal branching exponents across different scales can improve the functional assessment of organs.

Index Terms—Branching exponents, Fåhræus–Lindqvist effect, human liver, Murray’s law, synthetic vascular trees, vascular corrosion cast.

I. INTRODUCTION

THE cardiovascular system is responsible for transporting blood to and from all cells in the human body, leading to

Manuscript received 27 September 2023; revised 31 October 2023; accepted 13 November 2023. Date of publication 20 November 2023; date of current version 21 March 2024. This work was supported by the European Research Council (ERC) through the European Union’s Horizon 2020 Research and Innovation Programme under Grant 759001, achieved as part of the ERC Starting grant Project ‘ImageToSim’. (Corresponding author: Etienne Jessen.)

Etienne Jessen is with the Institute for Mechanics, Computational Mechanics Group, Technical University of Darmstadt, 64289 Darmstadt, Germany (e-mail: etienne.jessen@tu-darmstadt.de).

Marc C. Steinbach is with the Institute of Applied Mathematics, Leibniz University Hannover, Germany.

Charlotte Debbaut is with IBItech-Biommeda, Ghent University, Belgium.

Dominik Schillinger is with the Institute for Mechanics, Computational Mechanics Group, Technical University of Darmstadt, Germany.

Digital Object Identifier 10.1109/TBME.2023.3334758

hierarchical networks of vessels, called vascular trees, inside each organ. According to Murray [1], this hierarchy obeys scaling relations based on the minimization of the total energy expenditure of the system. Many factors influence and constrain this minimization process, such as the type and shape of the organ supplied, the demand for the organ’s cells, and the existence of vascular diseases. The goals and constraints guiding their structural development and influence on the vascular system have yet to be entirely understood, even though extensive work has been carried out for over a century. Thus the analysis of vascular diseases based on the anatomy and physiology of the vascular structure remains a challenge.

Murray first described a minimization problem for vascular segments in 1926 [1], [2]. Here, a single artery (or capillary) is considered, modeled as a rigid cylindrical tube, and the physical principles for fluid flow follow Poiseuille’s law. The goal is to minimize the total power of the vessel, which results (among other relations) in Murray’s law. It describes the relationship of the radius of a parent vessel r_0 against the radii of its children’s vessels (r_1, \dots, r_n) as a power law with

$$r_0^\gamma = r_1^\gamma + \dots + r_n^\gamma. \quad (1)$$

The branching exponent γ became an essential parameter for characterizing the branching behavior of vascular trees. In his original formulation, Murray derives (1) with $\gamma = 3$ mathematically for a single branching and notes that it “tends to hold also in *small trees*” [2, p. 838].

An extensive number of studies have been conducted to investigate Murray’s law experimentally [3], [4], [5]. In general, exponents between 2.0 and 3.0 were measured. In [6], exponents were observed even going over Murray’s value of 3 with $\gamma = 3.2$. Multiple theoretical studies have analyzed the possible factors contributing to these branching behaviors. An extension to Murray’s law was proposed by Uylings [7], which incorporated the effects of turbulent flow into the minimization problem. Results show branching exponents as low as 2.33 for turbulent flow. In [8], a vascular model was investigated, which considered the role of elastic tubes. Compared to rigid tubes, the effect of pulsatile flow lowered the optimal value to 2.3. Zhou, Kassab, and Molloy [9], [10] generalized Murray’s law hypothesis to an entire coronary arterial tree by defining a vessel segment as a stem and the tree distal to the stem as a crown. They showed that γ deviates from 3.0 even for steady-state flow and depends on the ratio between metabolic demand and viscous power dissipation.

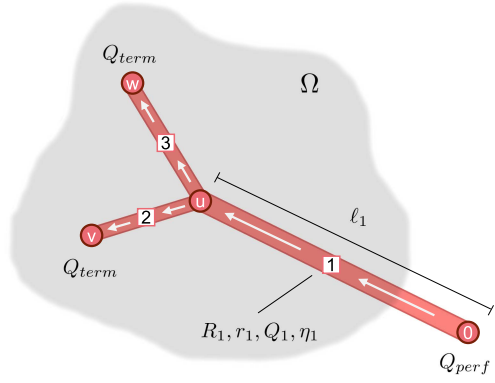


Fig. 1. Schematic of a vascular tree and its relation to nodes and segments. Red circles denote a node, and white rectangles a segment. This tree has a given inflow $Q_1 = Q_{\text{perf}}$ and equal terminal outflow $Q_2 = Q_3 = Q_{\text{term}}$ through each of the outlets (leaves). Arrows indicate the flow direction from the root node to the terminal nodes. All terminal nodes are inside the (non-convex) perfusion domain Ω .

An alternative approach to investigate the effects of different branching exponents is to construct vascular trees synthetically. The most well-known generation method here is constrained constructive optimization (CCO) [11]. This local optimization approach is directly based on Murray's minimization principles and allows to investigate different, albeit constant, values for γ , like 2.55 [12] or 3.0 [13]. Another approach, based on Simulated Annealing (SA), included a (single) branching exponent as an optimization variable [14]. Results show that the vascular topology and the metabolic demand significantly influence the value of the branching exponent. Recently, we extended the CCO approach to finding a synthetic tree optimal both in (global) geometry and topology [15]. Finding the optimal geometry is cast into a nonlinear optimization problem (NLP), which allows the investigation of various possible goal functions and constraints.

In this work, we utilize the flexibility of our global optimization framework and go beyond previous studies by allowing the branching exponent γ to vary locally. We consider Murray's law to hold if in fact all values coincide. Our goal is to investigate how the optimal branching exponents change under different optimality principles. Firstly, we extend Murray's original problem by constraining the pressure drop to be equal from the root to every terminal node. This constraint is widely used for generating synthetic vascular trees (see [11], [12], [15], [16]) but was not part of Murray's original formulation. Secondly, we include a blood viscosity law based on the Fåhræus–Lindqvist effect [17]. Since we generate vascular trees with one million terminal vessels, going further than previous studies [18], this change in apparent blood viscosity becomes significant.

We start by introducing the relevant definitions and assumptions to generate synthetic trees. We then cast our goals and constraints into NLPs and introduce our optimization framework and its limitations in more detail. Finally, we generate full portal venous trees of the human liver with up to one million terminal vessels and compare them against a vascular corrosion cast of a human liver [19], [20].

II. METHODS

A. Definitions and Assumptions

We represent a vascular tree as a directed branching network $\mathbb{T} = (\mathbb{V}, \mathbb{A})$ with nodes $u \in \mathbb{V}$ and segments $a \in \mathbb{A}$. Each segment $a = uv$ connects a proximal node x_u with a distal node x_v . It approximates a vessel as a rigid and straight cylindrical tube and is defined by its radius r_a , length $\ell_a = \|x_u - x_v\|$, volumetric flow Q_a and apparent blood viscosity η_a . The distal nodes of *terminal segments* are terminal nodes (*leaves*) $v \in \mathbb{L}$, and the proximal node of the (single) *root segment* is the root node x_0 . A synthetic vascular tree perfuses blood at a steady state from the root segment down to the terminal segments inside a given (non-convex) perfusion volume $\Omega \subset \mathbb{R}^3$, schematically shown in Fig. 1.

As in Murray's original paper [1], we assume laminar flow and approximate blood as an incompressible homogeneous Newtonian fluid. We express the hydrodynamic resistance R_a of segment a by Poiseuille's law with

$$R_a = \frac{8\eta_a \ell_a}{\pi r_a^4} \quad \forall a \in \mathbb{A}. \quad (2)$$

The pressure drop over a segment can now be computed as

$$\Delta p_a = R_a Q_a \quad \forall a \in \mathbb{A}, \quad (3)$$

and the pressure at a node v follows with

$$p_v = p_u - \Delta p_a \quad \forall uv \in \mathbb{A}. \quad (4)$$

We further assume that the (known) perfusion flow Q_{perf} is homogeneously distributed among all N terminal segments, leading to a terminal flow value $Q_{\text{term}} = Q_{\text{perf}}/N$. All remaining flow values can then be computed using Kirchhoff's law with $Q_{uv} = \sum_{vw \in \mathbb{A}} Q_{vw} \forall v \in \mathbb{V} \setminus (0 \cup \mathbb{L})$.

We aim at generating vessels down to the smallest arterioles/venules with typical radii in the range of 0.015 mm to 0.1 mm. The Fåhræus–Lindqvist effect [21] should be accounted for at this scale. It describes how the blood viscosity decreases as the vessel diameter decreases. The tendency of red blood cells to migrate toward the vessel center is largely responsible for this effect. In turn, this forces plasma toward the walls and decreases peripheral friction. At the smallest vessels with radii approaching the radii of red blood cells, the viscosity sharply rises again. Pries et al. [17] derived an empirical relationship for this behavior with

$$\eta(r_a) = \eta_p (\kappa + \kappa^2 (\eta_{45} - 1)), \quad (5)$$

$$\eta_{45} = A \exp(Br_a) - C \exp(Dr_a^E) + F, \quad (6)$$

$$\kappa = \frac{r_a^2}{(r_a - G)^2}, \quad (7)$$

where η_p is the viscosity of the plasma, which we set to $\eta_p = 1.125$ cP. η_{45} is the relative apparent blood viscosity for a discharge hematocrit of 0.45. The values of the constants A to G are summarized in Table I.

TABLE I
NUMERICAL VALUES OF THE EMPIRICALLY DERIVED CONSTANTS FOR THE FÄHRÆUS–LINDQVIST EFFECT, AS DESCRIBED BY [17]

Parameter	Value	Unit
A	6.0	1
B	-170.0	mm ⁻¹
C	2.44	1
D	-8.08	mm ^{-E}
E	0.645	1
F	3.2	1
G	0.00055	mm

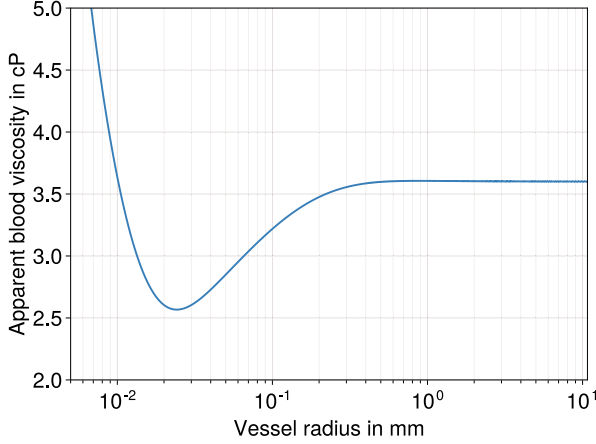


Fig. 2. Change in apparent blood viscosity due to the Fähræus–Lindqvist effect as approximated by Pries et al. [17].

This relationship is depicted in Fig. 2 for the relevant radii between 0.015 mm and 10 mm.

B. Design Goals and Constraints

1) Murray’s Minimization Problem: The original minimization formulation by Murray states that the total power of a vascular tree consists of the metabolic power required to sustain blood P_{vol} and the viscous power P_{vis} required to pump blood from the root down to the micro-circulation. The cost function of a tree is then defined as

$$f_{\mathbb{T}} = P_{\text{vol}} + P_{\text{vis}} = \sum_{a \in \mathbb{A}} m_b \pi \ell_a r_a^2 + \frac{8\eta_a \ell_a}{\pi r_a^4} Q_a^2, \quad (8)$$

where m_b is the metabolic demand of blood in μWmm^{-3} . As described in [15], we can now include the nodal positions x , the lengths ℓ and radii r as well as the blood viscosities η in the vector of optimization variables y_1 , leading to $y_1 = (x, \ell, r, \eta)$. We add physical lower bounds ℓ^- , r^- and η^- and, for numerical efficiency, upper bounds ℓ^+ , r^+ and η^+ . The best geometry is then found in the rectangle defined as

$$Y_1 = \mathbb{R}^{3|\mathbb{V}|} \times [\ell^-, \ell^+]^{\mathbb{A}} \times [r^-, r^+]^{\mathbb{A}} \times [\eta^-, \eta^+]^{\mathbb{A}}. \quad (9)$$

Our NLP “Power minimization” finally reads:

$$\min_{y_1 \in Y_1} \sum_{a \in \mathbb{A}} m_b \pi \ell_a r_a^2 + \frac{8\eta_a \ell_a}{\pi r_a^4} Q_a^2 \quad (10)$$

$$\text{s.t. } 0 = x_u - \bar{x}_u, \quad u \in \mathbb{V}_0 \cup \mathbb{L}, \quad (11)$$

$$0 = \ell_{uv}^2 - \|x_u - x_v\|^2, \quad uv \in \mathbb{A}, \quad (12)$$

$$0 = \eta_a - \eta(r_a), \quad a \in \mathbb{A}. \quad (13)$$

Eq. (11) fixes the position of terminal nodes and (12) ensures consistency between nodal positions and segment length. The third constraint in (13) enforces the Fähræus–Lindqvist effect as defined in (5). Without this constraint, the NLP describes the original minimization problem of Murray extended to an entire vascular tree, and hence we expect that every solution will satisfy Murray’s law with $\gamma = 3$.

2) Enforcing Equal Pressure Drop: In Murray’s original formulation, no consideration of the resulting pressure values at terminal segments was given. This terminal pressure is a crucial parameter for the regulation of blood flow and blood velocity at the microcirculatory domains. Since we assume these domains are roughly homogeneous across the organ and have equal demand, the pressure should not differ significantly. Therefore we enforce equal pressure at each terminal segment by adding the pressure p_v at each node as a new unknown in our (second) NLP with variables $y_2 = (x, \ell, r, \eta, p)$, leading to

$$Y_2 = \mathbb{R}^{4|\mathbb{V}|} \times [\ell^-, \ell^+]^{\mathbb{A}} \times [r^-, r^+]^{\mathbb{A}} \times [\eta^-, \eta^+]^{\mathbb{A}}. \quad (14)$$

Secondly, we constrain the pressure drop between the root and the terminal nodes as a prescribed constant value Δp . Since the viscous power at each segment a is directly proportional to the pressure drop by a factor of Q_a , the total viscous power P_{vis} becomes a constant. Thus, we can remove it from the cost function. Finally, we can drop the constant factor m_b , leading to a minimization goal proportional to the tree volume $V_{\mathbb{T}}$. This formulation is used in most synthetic tree studies, e.g., [11], [12], [14], [15], [16]. Our NLP “Volume minimization” then reads:

$$\min_{y_2 \in Y_2} \sum_{a \in \mathbb{A}} \pi \ell_a r_a^2 \quad (15)$$

$$\text{s.t. } 0 = x_u - \bar{x}_u, \quad u \in \mathbb{V}_0 \cup \mathbb{L}, \quad (16)$$

$$0 = \ell_{uv}^2 - \|x_u - x_v\|^2, \quad uv \in \mathbb{A}, \quad (17)$$

$$0 = p_u - p_v - \frac{8\eta_{uv} \ell_{uv}}{\pi r_{uv}^4} Q_{uv}, \quad uv \in \mathbb{A}, \quad (18)$$

$$0 = p_u, \quad u \in \mathbb{L}, \quad (19)$$

$$0 = p_0 - \Delta p, \quad (20)$$

$$0 = \eta_a - \eta(r_a) \quad a \in \mathbb{A}. \quad (21)$$

Remark 1: Murray’s law, as stated in (1), is again not enforced explicitly with a prescribed value of γ . Instead, we allow a different value at each node and compute the resulting branching exponent γ using the Newton-Raphson method after the optimization is finished.

3) Additional Optimization Variants: To better isolate the individual influence of different factors, we define additional

variants of our two minimization problems. Firstly, we simplify both problems to a constant apparent viscosity $\eta_{\text{const}} = 3.6$ cP, removing η from the vector of optimization variables and dropping the corresponding constraints (13) and (21). Secondly, we investigate the influence of the metabolic demand m_b and the total pressure drop Δp . We consider values between $0.1 \mu\text{W mm}^{-3}$ and $1.0 \mu\text{W mm}^{-3}$ for the metabolic demand, but note that estimates of this parameter vary significantly [22]. For the total pressure drop, we set the terminal pressure to $p_{\text{term}} = 6$ mmHg and vary the root pressure between 10 mmHg and 14 mmHg. Finally, for each variant, a separate tree is generated, where Murray's law (see (1)) is enforced directly with a single exponent γ_{opt} , included in the optimization variables. All variants include the same root flow $Q_{\text{perf}} = 1.1 \text{ L min}^{-1}$. We note that in our tests different values of Q_{perf} had no significant effect on the branching behavior between vessels and only led to different scaling of the vessel radii.

C. Applicability to Vascular Systems

Before we describe our generation framework in more detail, we discuss its limitations. Specifically, how the assumptions of Section II-A limit the applicability of our framework for certain types of vessels.

First, the assumption of a tree-structured network only holds down to the entry of the microcirculation (vessels with radii between $15 \mu\text{m}$ to $35 \mu\text{m}$). From here, the tree structure transmutes into a mesh-like network of capillaries, which is not covered by our current model.

Second, the assumption of Poiseuille flow constitutes a strong limitation on the type of vessels we can adequately describe. The pulsatility introduced by the heartbeat can hinder the flow from fully developing a parabolic velocity profile. The significance of this effect is characterized by the dimensionless Womersley number α [23] for each vessel a with

$$\alpha_a = r_a \left(\frac{\omega \rho}{\eta_a} \right)^{\frac{1}{2}}, \quad (22)$$

where ω is the angular frequency and ρ the density of blood. At Womersley numbers over 10, the flow lags behind the pressure wave by approximately 90 degrees, and the velocity profile has a plug-like shape [24]. This effect can only be neglected for Womersley numbers under 1. Assuming constant frequency and density, the Womersley number is mostly based on the radius of the vessel. For a resting heartbeat of 1 Hz and a blood density of 1000 kg m^{-3} vessels with radii over 8mm have significant pulsatile effects, whereas vessels with radii under 1mm can be assumed to allow Poiseuille flow to develop fully. Thus for vascular trees, pulsatile effects are only significant at root vessels but quickly diminish after only 3 to 4 consecutive branches. For these first branches, however, the additional energy dissipation introduced by the pulsatile flow is again not covered by our current model.

Lastly, we assume a homogeneous distribution of flow (in all cases) and an equal pressure drop to each terminal node (in the case of "Volume minimization"). In reality, this assumption will not hold, even for healthy organs, as different parts of the organ

will be perfused differently. While it is not part of this study, we wish to point out that the algorithm is capable of including arbitrary heterogeneous distributions of flow and pressure drops. However, localized effects like arterial dilation caused by, e.g., limited oxygen supply, are not accounted for in our current model and should be part of further studies.

D. Generation Framework

We generate our synthetic trees using the framework introduced in [15], which we summarize in the following. First, we generate N_{topo} terminal nodes on a regular cubic grid inside our organ's volume. The root position is manually set and connected to the geometric center of the volume, which in turn is connected to all terminal nodes. We swap segments to explore new topologies from this initial (fan-shaped) tree. A *swap* detaches a segment from its parent and connects it with another segment. After each swap, the geometry is optimized by solving the corresponding NLP. The newly created topology is accepted on the basis of an SA approach. After topology optimization, we grow the tree using a modified CCO approach. Here, we optimize the global geometry each time after adding N_{geo} new terminal nodes and then increase N_{geo} heuristically based on the current density of the tree. Notably, we drop the local optimization of branching positions and set them to their flow-weighted mean, similar to [25]. Due to our repeated global geometry optimization, this simplification has no significant impact on the final tree structure. In the last step of the optimization, we delete all segments that reached the lower bound ℓ^- (*degenerate segments*), possibly creating n -furcations ($n \geq 3$).

We then classify the hierarchy throughout the finished tree by assigning each segment an order number corresponding to the Strahler ordering method [26]. Leaf nodes are assigned the order 1. Then, going upstream, parent nodes are assigned a Strahler order according to the following rule: A parent node is assigned the maximum order of its children. If all children have the same order, the parent is assigned the order of its children plus 1.

Remark 2: The complete optimization framework is only applied once to obtain a common topology. We solve each NLP variant with this topology to get the corresponding global geometry. We chose this method to focus on the geometry changes and to allow a direct comparison of branching exponents and radii at the same branch types.

III. RESULTS

A. Computational Complexity

We first investigate the computational complexity of our framework, which can be formally divided into a growth part based on CCO and an optimization part based on the NLPs. As described in more detail in [25], one can achieve polynomial complexity in the number of terminal nodes N for CCO by using the tree as a binary search tree to connect new terminal points efficiently. We further reduce the computational effort by setting the new branch location to the flow-weighted mean instead of computing the local optimum. These design decisions

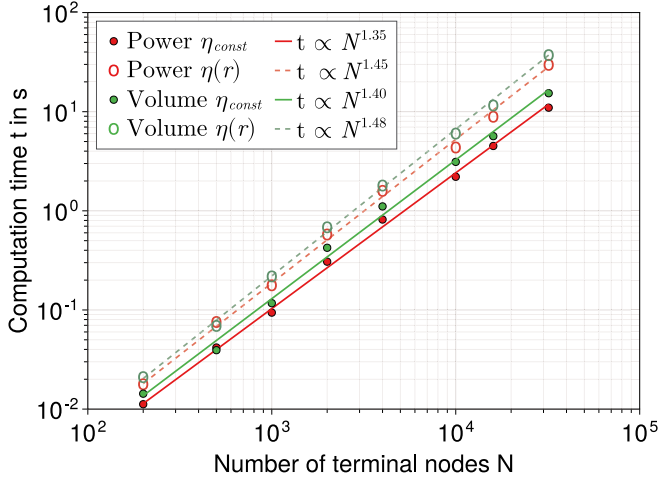


Fig. 3. Computation time and estimated polynomial scaling of the different NLP variants. Each measurement constitutes the median of 100 test computations.

allow us to grow a synthetic tree up to the microcirculation. Thus, the most critical part of the framework is the optimization part, which consists of the geometry optimization during growth and the topology optimization of the initial tree. During topology optimization, each iteration consists of swapping two segments and globally optimizing the new geometry. Each swap between two segments only requires updates along the path up to the lowest common ancestor. This part of the algorithm scales at worst linearly, and the performance of the topology optimization depends on the performance of solving the NLP, which we investigate in the following.

We solve the NLPs using the interior point code *Ipopt* [27] with the linear solver *Mumps* [28]. All computations are executed on a desktop computer with 64 GB of random-access memory (RAM) and an AMD Ryzen 9 7950X @5Ghz processor with 32 threads. The computation times of our NLPs for different numbers of terminal segments are depicted in Fig. 3. It is apparent that the solution effort for all NLP variants scales polynomially with N , in fact even superlinearly with moderate exponents below 1.5. Power minimization performs best as it has the fewest number of optimization variables and constraints. The inclusion of equal pressure and the Fåhræus–Lindqvist effect both lead to higher computation times. To estimate the performance gain that we achieve by dropping Murray’s law, we include it as a constraint in the NLP “Volume minimization”, both with the fixed branching exponent $\gamma = 3$ and with a single value γ left free for optimization. The resulting computation times are shown in Fig. 4. Enforcing Murray’s law increases the solution effort substantially. Moreover, it leads to larger complexity exponents, which becomes significant during topology optimization and for denser trees.

For instance, the computation time for solving the “Volume minimization” NLP with 1,000,000 terminal segments almost doubles from approximately 65 min to 118 min when including Murray’s law.

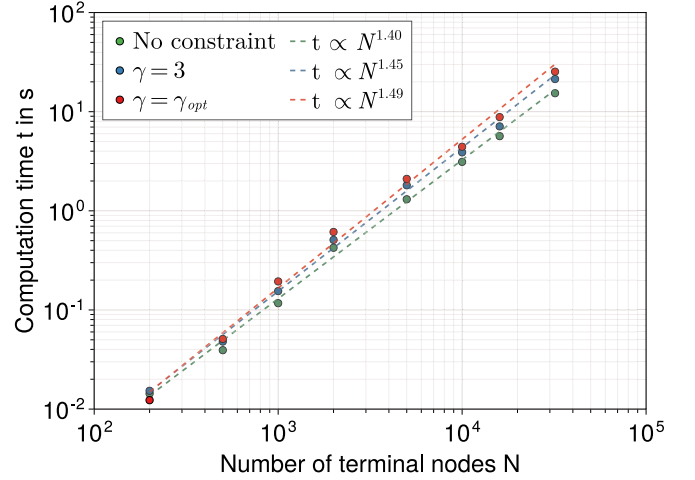


Fig. 4. Effects on computation time and scaling when directly enforcing Murray’s law with fixed and variable γ for the case of “Volume minimization” with constant blood viscosity. Each measurement constitutes the median of 100 test computations.

B. Overall Structure of the Synthetic Portal Vein

The full synthetic portal vein tree for the case of “Volume minimization” with variable viscosity is depicted in Fig. 5. The perfusion volume of the liver was around 1.500 cm³ and we used physiological parameters adapted from [16], namely a total pressure drop of $\Delta p = 4$ mmHg and a root inflow of $Q_{\text{perf}} = 1.1$ L min⁻¹. The left side shows the complete tree inside the non-convex liver domain with two zoom levels. The tree splits into four major branches, which further split into 8 main branches. These results align with previous results of a sparser tree in [15] and highlight that the removal of Murray’s law and the inclusion of the Fåhræus–Lindqvist effect have only a minor influence on the topology of the major vessels.

For a detailed comparison between the different optimization variants discussed in Section II-B3, we summarized the results in Table II. Here, a column represents the results of a single variant, with the first four columns corresponding to the NLP “Power minimization” and the last four columns corresponding to the NLP “Volume minimization”. For “Power minimization”, we included the results for metabolic demands m_b of 0.1 μWmm^{-3} and 1.0 μWmm^{-3} . Similarly, for “Volume minimization”, we included the results for root pressures p_{root} of 10 mmHg and 14 mmHg. The last row indicates the results of each variant after enforcing a single (optimal) branching exponent γ_{opt} .

For “Power minimization”, an increase in metabolic demand m_b from 0.1 μWmm^{-3} to 1.0 μWmm^{-3} leads to an increase in viscous power P_{vis} , shown in the first row of Table II, by around 364% and a reduction in volume V_{T} , shown in the second row Table II, by around 53%. Similarly, for the “Volume minimization”, an increase in the root pressure from 10 mmHg to 14 mmHg leads to a 320% increase in viscous power and a 51% reduction in volume. The Fåhræus–Lindqvist effect had a minor influence. It decreased the viscous power by around 1% and the total volume by around 4% in all cases.

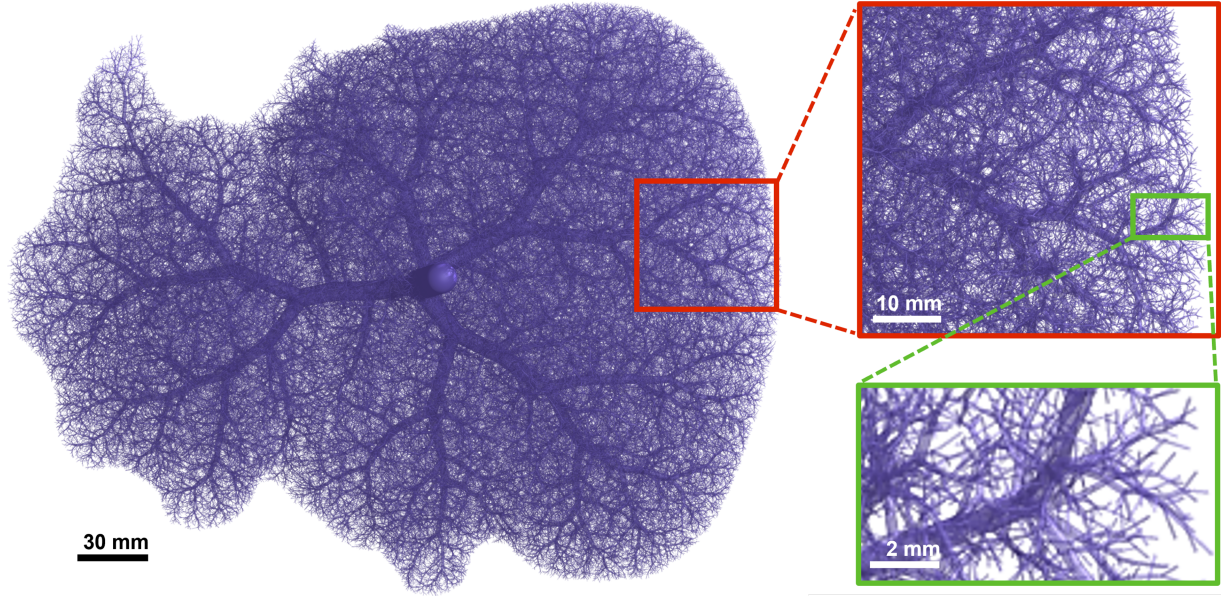


Fig. 5. Complete synthetic vascular tree of the portal vein of a human liver with 1,000,000 terminal vessels (“Volume minimization” with variable viscosity and $p_{\text{root}} = 10$ mmHg). Two zoom levels highlight the hierarchical structure at different scales. The radii are between 5.1 mm (root vessel) and 0.017 mm (smallest terminal vessel).

TABLE II
COMPARISON OF THE RESULTS BETWEEN THE DIFFERENT VARIANTS OF OUR TWO MINIMIZATION PROBLEMS AS INTRODUCED IN SECTION II-B3

Parameter	Power minimization				Volume minimization			
	$m_b = 0.1 \mu\text{W mm}^{-3}$		$m_b = 1.0 \mu\text{W mm}^{-3}$		$p_{\text{root}} = 10.0 \text{ mmHg}$		$p_{\text{root}} = 14.0 \text{ mmHg}$	
	η_{const}	$\eta(r)$	η_{const}	$\eta(r)$	η_{const}	$\eta(r)$	η_{const}	$\eta(r)$
P_{vis} in mW	2.67	2.65	12.34	12.23	3.33	3.33	13.99	13.99
V_{T} in mm^3	53,400.60	52,283.94	24,786.36	24,042.08	50,413.84	49,158.58	24,587.02	23,154.13
r_{root} in mm	5.35	5.35	3.64	3.63	5.10	5.09	3.56	3.54
p_{term} in mmHg	[10.34, 11.68]	[10.41, 11.73]	[1.15, 10.67]	[1.74, 10.98]	6.00	6.00	6.00	6.00
γ	3.00	[2.90, 3.00]	3.00	[2.90, 3.00]	[1.75, 3.01]	[1.76, 3.17]	[1.43, 3.00]	[1.46, 3.08]
γ_{opt} (constant)	3.00*	2.91*	3.00*	2.92*	2.84*	2.76*	2.82*	2.74*

The branching exponents γ_{opt} in the last row (marked with *) are the results of separate runs for each variant, where a single constant branching exponent was enforced.

C. Vessel Radii

The root radius r_{root} is shown in the third row of Table II. It decreased by 31% after the metabolic demand m_b was increased for “Power minimization”. Similarly, in the case of “Volume minimization”, it decreased by 30% after the root pressure p_{root} was increased to 14 mmHg. In all cases, the Fåhræus–Lindqvist effect had a minor influence on the root radius with changes less than 0.1%. However, a significant decrease in radius can be observed for vessels between Strahler orders 1 and 6, shown in Fig. 6. In both NLP cases, this decrease was highest at the terminal vessels with 2% for “Power minimization” (Fig. 6(a)) and 1.5% for “Volume minimization” (Fig. 6(b)). A notable difference between both cases is the variance of radii at each Strahler order. In the case of “Power minimization”, the highest variance is observed at Strahler order 6, whereas the terminal radii are constant. In the case of “Volume minimization”, the highest variance is at the terminal segments and decreases as the Strahler order increases.

D. Pressure Drop

After “Power minimization”, the terminal pressures are not constant across the tree but exhibit a wide range of values, see Table II row 4 column 1–4. This range widens further for higher metabolic demands and also increases the mean total pressure drop from the root to the terminal segments, shown in Fig. 7. In Fig. 8(a), the pressure values at different Strahler orders are shown for $m_b = 0.1 \mu\text{W mm}^{-3}$. Pressure values drop and variances increase with decreasing Strahler order. Including the Fåhræus–Lindqvist effect leads to slightly higher pressure values for the Strahler orders 1 to 6. The terminal pressures after “Volume minimization” are fixed to $p_{\text{term}} = 6$ mmHg as enforced by (18)–(20). The effect of these constraints is highlighted in Fig. 8(b) for root pressure $p_{\text{root}} = 10$ mmHg. In contrast to “Power minimization”, variances are significantly higher at the intermediate Strahler orders 3 to 11. Furthermore, the influence of the Fåhræus–Lindqvist effect is more pronounced, decreasing the pressure values between Strahler order 2 to 10.

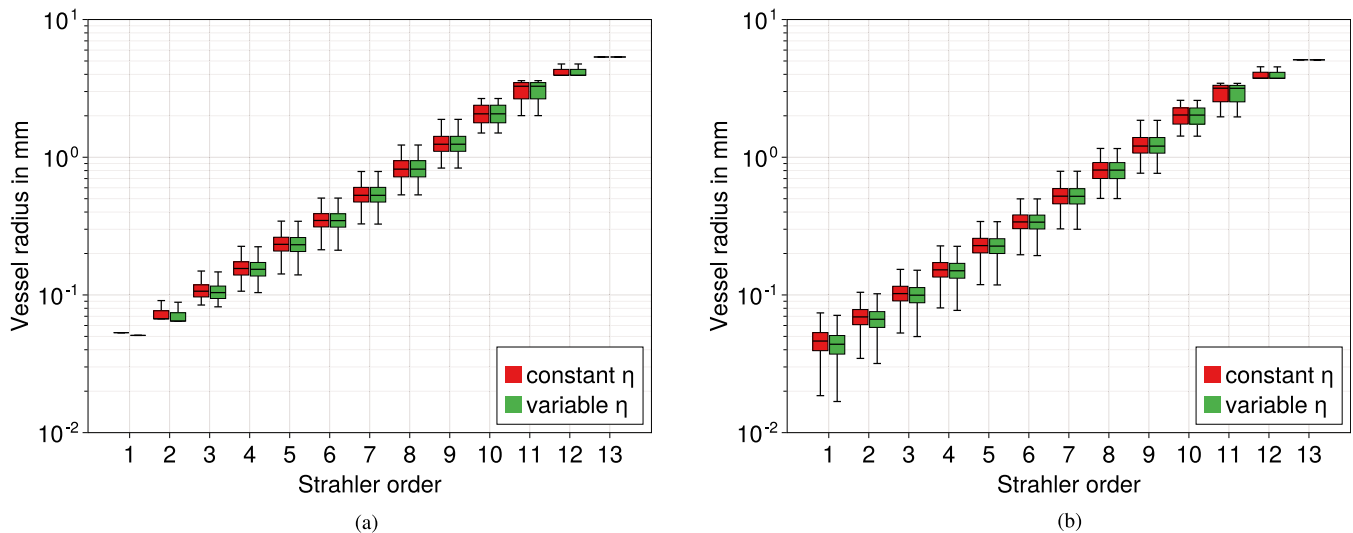


Fig. 6. Influence of Fåhræus–Lindqvist effect on vessel radii for different Strahler orders. (a) Power minimization ($m_b = 0.1 \mu\text{W mm}^{-3}$). (b) Volume minimization ($p_{\text{root}} = 10 \text{ mmHg}$).

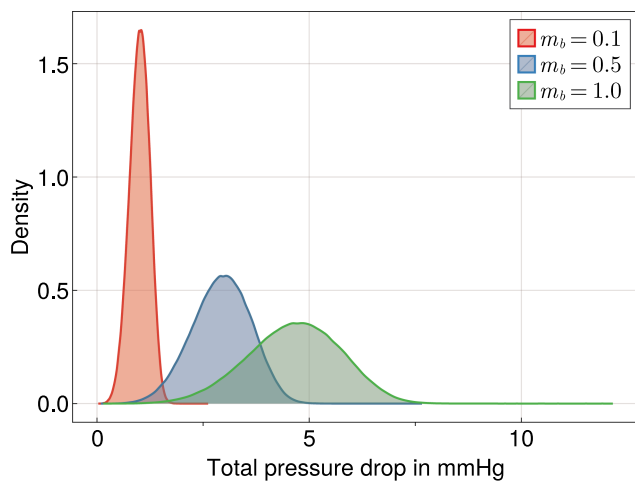


Fig. 7. Density plot of the total pressure drop from root vessel to terminal vessels for the power minimization under different metabolic demand.

E. Branching Behavior

The resulting branching exponents of all variants are summarized in row 5 of Table II. For “Power minimization” with constant viscosity η_{const} , the exponents are constant with $\gamma = 3.0$ across all branches regardless of metabolic demand m_b . This confirms our expectation, and it can easily be proved by standard theory using a certain separability property of the NLP. In contrast, the inclusion of the Fåhræus–Lindqvist effect leads to deviations from 3.0, with branching exponents reaching a minimum of 2.9. For “Volume minimization,” exponents are not constant even for constant blood viscosity because the pressure constraints introduce global coupling conditions across the tree. Instead, most values fall between 2.0 and 3.0, with the smallest outliers having values of 1.43.

For a more detailed comparison, the probability density function of the branching exponents for both optimization cases is

compared in Fig. 9. The influence of the Fåhræus–Lindqvist effect shifts most branching exponents from a constant 3.0 to 2.9 during “Power minimization” (Fig. 9(a)). During “Volume minimization” with constant blood viscosity, most exponents are at 3.0 (Fig. 9(b) in red) and are shifted to 2.9 when including the Fåhræus–Lindqvist effect (Fig. 9(b) in green).

Fig. 10 highlights the distribution of mean branching exponents across different branch types. Each cell (i, j) corresponds to a branch with child segments of Strahler order i and j . In Fig. 10(a) the effect of variable blood viscosity on “Power minimization” is depicted. The branching exponents decrease if the Strahler order of either child decreases, leading to the smallest branching exponent of 2.9 at branches with two terminal segments. If both child segments have a Strahler order over 8, the mean branching exponent is at its maximum of 3.0. The effect of enforcing equal terminal pressure is shown in Fig. 10(b). Here, the higher the difference between the Strahler orders of both children is, the smaller the branching exponent is. Again, the smallest mean branching exponents are observed at branches connecting two terminal segments with a value of 2.76. Fig. 10(c) shows the accumulated effect of both constraints with a minimum mean exponent of 2.7, again at terminal branches.

F. Comparison to Vascular Corrosion Cast

We now directly compare our synthetic trees against a corrosion cast of the portal vein of the human liver [20]. The corrosion cast was imaged at a resolution of $102 \mu\text{m}$, which allowed to recover vessels down to approximately 0.5 mm. Further imaging was done on a smaller sample (about $88 \times 68 \times 80 \text{ mm}$) at a resolution of $71 \mu\text{m}$. For this sample, vessels down to a diameter of approximately 0.08 mm were recovered. More detailed information on the human liver, vascular corrosion casting, and micro-CT scanning can be found in [19]. To allow a direct comparison between our synthetic data and the *generation* notation used for the vascular corrosion cast in [20], we employ an ordering scheme based on [4].

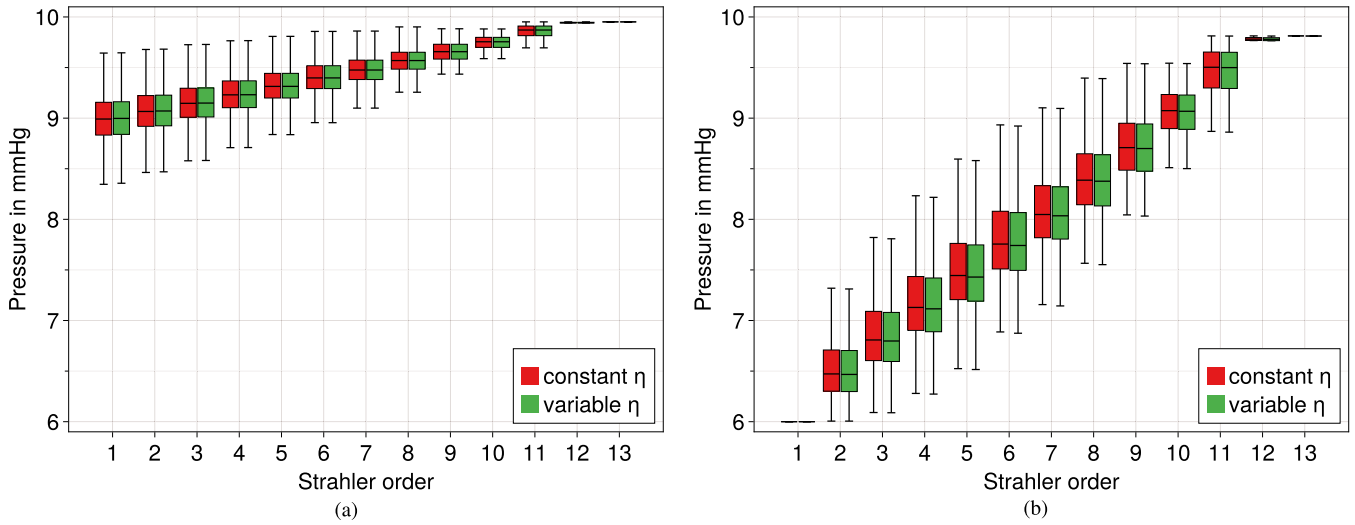


Fig. 8. Influence of Fåhræus–Lindqvist effect on pressure values of the distal nodes of vessels for different Strahler orders. (a) Power minimization ($m_b = 0.1 \mu\text{W mm}^{-3}$). (b) Volume minimization ($p_{\text{root}} = 10 \text{ mmHg}$).

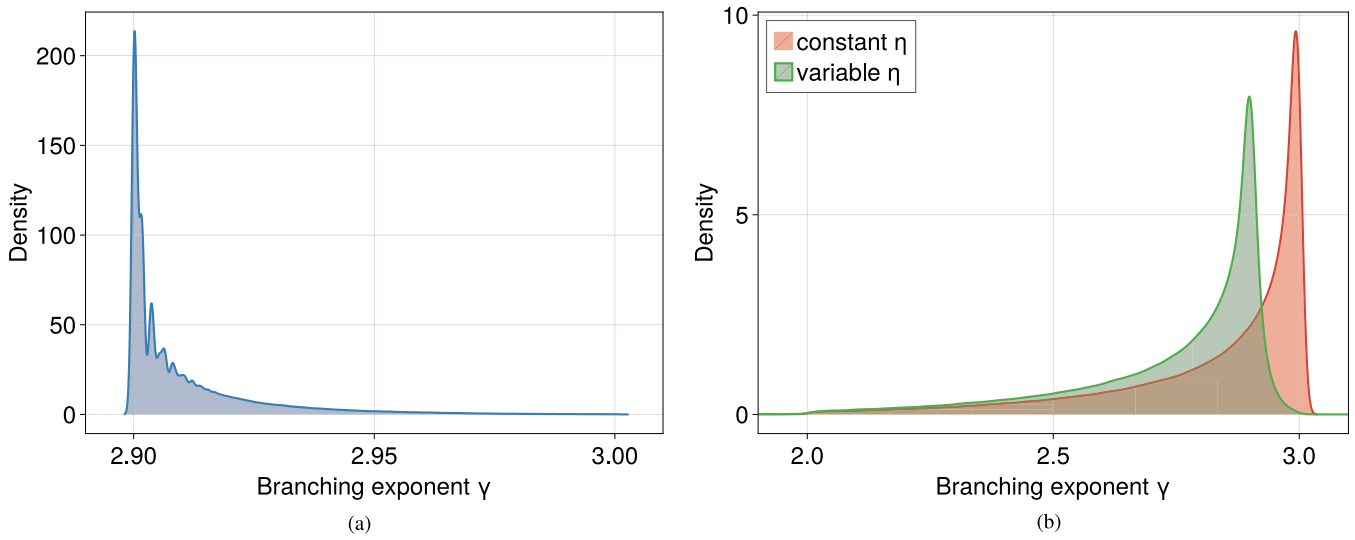


Fig. 9. Effect of enforcing variable viscosity and equal pressure onto the branching exponents. (a) Power minimization ($m_b = 0.1 \mu\text{W mm}^{-3}$). (b) Volume minimization ($p_{\text{root}} = 10 \text{ mmHg}$).

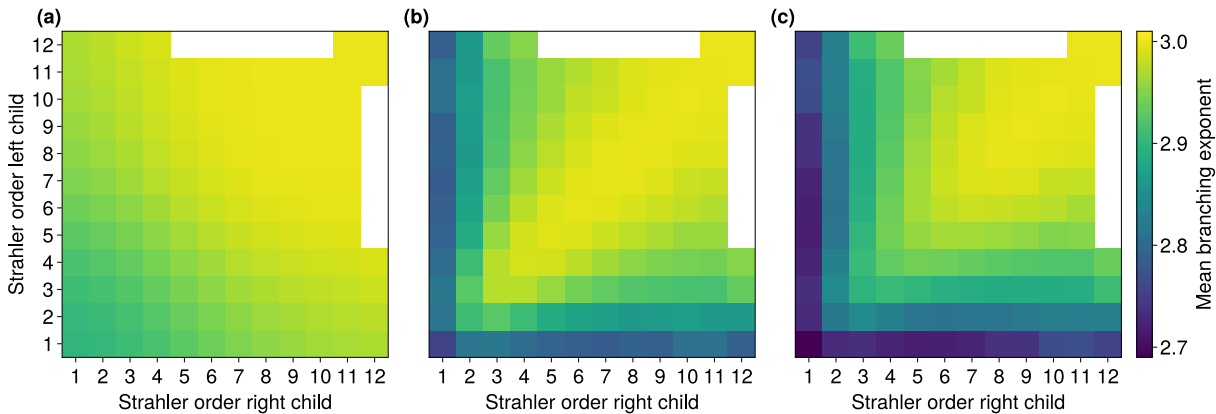


Fig. 10. Mean values of branching exponent γ for different types of branches, e.g., the cell (1,2) corresponds to branches, where child vessels of Strahler order 1 and 2 meet. The results are symmetric. White cells correspond to branch types, which do not occur in the tree topology. (a) Power minimization with variable viscosity, (b) volume minimization with constant viscosity, (c) volume minimization with variable viscosity.

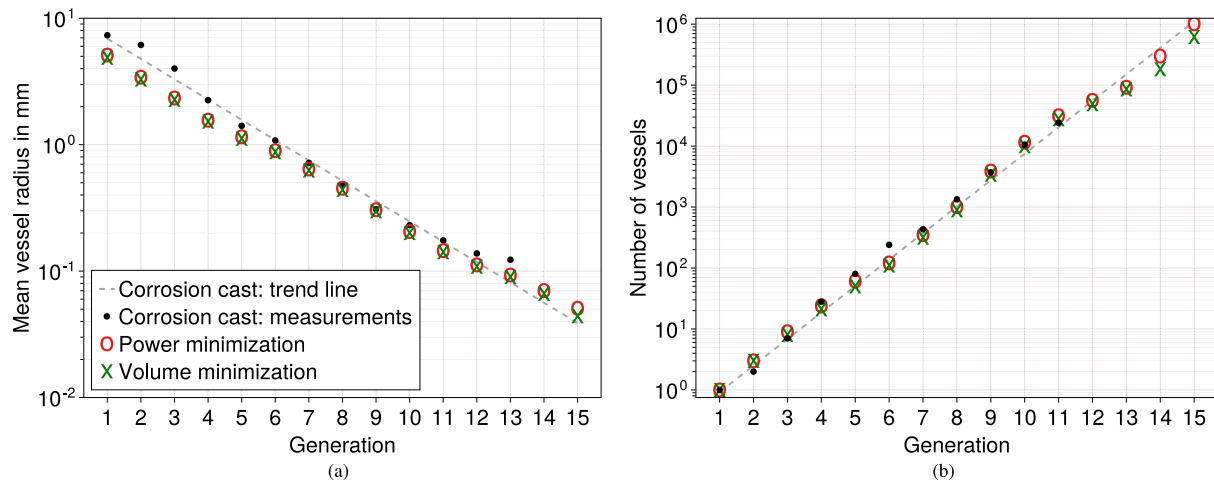


Fig. 11. Comparison of synthetic trees (with variable viscosity) against corrosion cast data [20]. (a) Mean radii. (b) Number of vessels.

In Fig. 11(a), the radii per generation (radius-adjusted Strahler order in reverse) are compared between the “Power minimization” with $m_b = 0.1 \mu\text{Wmm}^{-3}$, the volume minimization with $p_{\text{root}} = 10 \text{ mmHg}$ and the corrosion cast data, including measurements and a best-fit trend line, based on the least sum of square errors. The synthetic trees’ radii fit the data and trend line well for the generations 5 to 15. Notably, they significantly deviate for the first four generations, especially against the measurements with errors of around 25%. In contrast, the number of vessels in Fig. 11(b) of both synthetic trees fit the data of the corrosion cast well for all generations.

IV. DISCUSSION

The exclusion of Murray’s law simplifies our two optimization problems and automatically allows the branching exponents to vary locally. Both problems can generate synthetic trees with similar geometry and topology, if the parameters are chosen appropriately. Different parameter choices can change the final tree significantly, most notably due to the change in vessel radii. A higher root flow Q_{perf} increases the viscous power required to pump blood (right summand (10)) and the pressure drop at each vessel (18). In both cases, this leads to an increase in vessel radii. A higher blood viscosity leads to similar behavior as it also increases the viscous power and the pressure drop at each vessel. For Power minimization, we choose the metabolic factor m_b to be the same at each vessel. Thus, different values for m_b do not influence the branching exponents. However, a higher value directly increases the total metabolic power to maintain blood (left summand (10)) and decreases vessel radii. A metabolic factor of $m_b = 0.1 \mu\text{Wmm}^{-3}$ leads to more realistic radii than a value of $1.0 \mu\text{Wmm}^{-3}$. This is in line with estimated values around $0.03 - 0.04 \mu\text{Wmm}^{-3}$ for venous trees [22], [29]. Similarly, a root pressure of $p_{\text{root}} = 14 \text{ mmHg}$ results in a pressure drop of $\Delta p = 8 \text{ mmHg}$, which is related to portal hypertension. To allow such a high pressure drop, the vessel radii need to be decreased to unrealistic small values. In comparison a root pressure of $p_{\text{root}} = 10 \text{ mmHg}$ leads to vessel radii,

which are comparable to measurements of the vascular corrosion cast.

Under power minimization, the radii are at their individual local optima, i.e., the radius of each segment can be solved independently as the minimum of the metabolic demand and the viscous power dissipation. This observation is in line with the findings of Murray and explains the constant branching exponent of 3 in Table II. The variations in radii for Strahler orders 2 to 12 in Fig. 6(a) are based entirely on the branching type, which is completely defined by the flow values of the child segments.

For volume minimization, no such simplification can be made, as the constraint of equal pressure creates dependencies between segments on the same path to the root. This constraint also forces radii to deviate from their local optima, which means a deviation from the branching exponent $\gamma = 3.0$. The highest deviations are found at branches between two terminal segments because they can be adjusted to a given pressure drop without significantly increasing the tree’s volume. Given the same length, they also constitute a higher pressure drop than segments with bigger radii.

The inclusion of the Fåhræus–Lindqvist effect reduces the viscosity of smaller vessels, which can lead to different viscosity values between a parent vessel and its children. Consequently, the corresponding branching exponents also deviate from $\gamma = 3.0$, as can be observed in Fig. 10. In contrast, the effect on bigger vessels is negligible and results in constant exponents $\gamma = 3.0$, as seen in Fig. 10(a), for branches where both children have Strahler orders over 8.

While the generated trees generally fit the corrosion cast data well, the underestimation of the largest radii (generation 1 to 4) is significant. One reason for this underestimation is likely that the vessels of the portal venous tree are not completely circular and elliptical [20]. A bigger amount of pressure is thus required to drive the same amount of flow through such an elliptical cross-section. A second reason could be the negligence of pulsatility, leading to smaller energy dissipation at the largest vessels of the synthetic tree. Despite the higher Womersley numbers at these early generations, however, we suspect that this dissipation has only a limited effect on the underestimation of the vessel radii.

V. CONCLUSION

Our optimization framework can handle complex constraints and goal functions while generating synthetic trees up to but not including the capillary level of the microcirculation. We used our framework to investigate the local branching behavior for different constraints and goal functions. Branching exponents automatically lie in the experimentally predicted range between 2.0 and 3.0. Even small changes to Murray's original optimization problem, like the inclusion of variable blood viscosity, significantly affect the optimal branching exponents of vessels. Our synthetic trees closely follow the vascular corrosion cast of a human portal venous tree, with significant deviations only in the largest vessels.

Without enforcing any pressure constraint, terminal pressures vary by up to 1.0 mmHg, leading to highly heterogeneous boundary conditions for the microcirculation. In contrast, enforcing equal terminal pressure in its current form leads to pressure variations up to 2.0 mmHg in the intermediate vessels of the mesocirculation. Both these results need to be critically evaluated and compared against measurements of real vascular trees. In the future, we plan to include pulsatile flow effects, improving our framework's computational ability. Furthermore, shear stress, a critical parameter for vascular growth, must also be incorporated into the model.

A more mature version of this model, specifically the ability to predict optimal branching exponents under different constraints, could have many potential applications in the medical field. An example would be to predict and relate the branching behavior across the scales to vascular diseases. These predictions could improve the interpretation of medical images by giving valuable input to the functional assessment of organs. Another application lies in the emerging field of tissue-engineered products [30]. Here, tissue is bio-printed and requires an optimal vascular tree to support its cells. Our framework would allow to construct these trees under various possible design goals and constraints.

REFERENCES

- [1] C. D. Murray, "The physiological principle of minimum work: I. The vascular system and the cost of blood volume," *Proc. Nat. Acad. Sci. United States Amer.*, vol. 12, no. 3, pp. 207–214, 1926.
- [2] C. D. Murray, "The physiological principle of minimum work applied to the angle of branching of arteries," *J. Gen. Physiol.*, vol. 9, no. 6, pp. 835–841, 1926.
- [3] K. Horsfield and M. J. Woldenberg, "Diameters and cross-sectional areas of branches in the human pulmonary arterial tree," *Anat. Rec.*, vol. 223, no. 3, pp. 245–251, 1989.
- [4] Z. Jiang, G. Kassab, and Y. Fung, "Diameter-defined Strahler system and connectivity matrix of the pulmonary arterial tree," *J. Appl. Physiol.*, vol. 76, no. 2, pp. 882–892, 1994.
- [5] E. VanBavel and J. Spaan, "Branching patterns in the porcine coronary arterial tree. Estimation of flow heterogeneity," *Circulation Res.*, vol. 71, no. 5, pp. 1200–1212, 1992.
- [6] Y. Nakamura and S. Awa, "Radius exponent in elastic and rigid arterial models optimized by the least energy principle," *Physiol. Rep.*, vol. 2, no. 2, 2014, Art. no. e00236.
- [7] H. Uylings, "Optimization of diameters and bifurcation angles in lung and vascular tree structures," *Bull. Math. Biol.*, vol. 39, no. 5, pp. 509–520, 1977.
- [8] P. R. Painter, P. Edén, and H.-U. Bengtsson, "Pulsatile blood flow, shear force, energy dissipation and Murray's law," *Theor. Biol. Med. Modelling*, vol. 3, no. 1, pp. 1–10, 2006.
- [9] Y. Zhou, G. S. Kassab, and S. Molloi, "On the design of the coronary arterial tree: A generalization of Murray's law," *Phys. Med. Biol.*, vol. 44, no. 12, 1999, Art. no. 2929.
- [10] G. S. Kassab, "Scaling laws of vascular trees: Of form and function," *Amer. J. Physiol.-Heart Circulatory Physiol.*, vol. 290, no. 2, pp. H894–H903, 2006.
- [11] W. Schreiner and P. F. Buxbaum, "Computer-optimization of vascular trees," *IEEE Trans. Biomed. Eng.*, vol. 40, no. 5, pp. 482–491, May 1993.
- [12] R. Karch et al., "A three-dimensional model for arterial tree representation, generated by constrained constructive optimization," *Comput. Biol. Med.*, vol. 29, no. 1, pp. 19–38, 1999.
- [13] W. Schreiner et al., "Heterogeneous perfusion is a consequence of uniform shear stress in optimized arterial tree models," *J. Theor. Biol.*, vol. 220, no. 3, pp. 285–301, 2003.
- [14] J. Keelan and J. P. Hague, "The role of vascular complexity on optimal junction exponents," *Sci. Rep.*, vol. 11, no. 1, pp. 1–14, 2021.
- [15] E. Jessen et al., "Rigorous mathematical optimization of synthetic hepatic vascular trees," *J. Roy. Soc. Interface*, vol. 19, no. 191, 2022, Art. no. 20220087.
- [16] M. Kretowski et al., "Physiologically based modeling of 3-D vascular networks and CT scan angiography," *IEEE Trans. Med. Imag.*, vol. 22, no. 2, pp. 248–257, Feb. 2003.
- [17] A. Pries et al., "Resistance to blood flow in microvessels in vivo," *Circulation Res.*, vol. 75, no. 5, pp. 904–915, 1994.
- [18] L. Cury et al., "Parallel generation of extensive vascular networks with application to an archetypal human kidney model," *Roy. Soc. Open Sci.*, vol. 8, no. 12, 2021, Art. no. 210973.
- [19] C. Debbaut et al., "From vascular corrosion cast to electrical analog model for the study of human liver hemodynamics and perfusion," *IEEE Trans. Biomed. Eng.*, vol. 58, no. 1, pp. 25–35, Jan. 2011.
- [20] C. Debbaut et al., "Analyzing the human liver vascular architecture by combining vascular corrosion casting and micro-CT scanning: A feasibility study," *J. Anatomy*, vol. 224, no. 4, pp. 509–517, 2014.
- [21] R. Fähræus and T. Lindqvist, "The viscosity of the blood in narrow capillary tubes," *Amer. J. Physiol.-Legacy Content*, vol. 96, no. 3, pp. 562–568, 1931.
- [22] Y. Liu and G. S. Kassab, "Vascular metabolic dissipation in Murray's law," *Amer. J. Physiol.-Heart Circulatory Physiol.*, vol. 292, no. 3, pp. H1336–H1339, 2007.
- [23] J. R. Womersley, "Method for the calculation of velocity, rate of flow and viscous drag in arteries when the pressure gradient is known," *J. Physiol.*, vol. 127, no. 3, 1955, Art. no. 553.
- [24] M. Zamir and R. Budwig, "Physics of pulsatile flow," *Appl. Mechanics Rev.*, vol. 55, no. 2, pp. B35–B35, 2002.
- [25] A. A. Guy et al., "3D printable vascular networks generated by accelerated constrained constructive optimization for tissue engineering," *IEEE Trans. Biomed. Eng.*, vol. 67, no. 6, pp. 1650–1663, Jun. 2020.
- [26] A. N. Strahler, "Quantitative analysis of watershed geomorphology," *Eos, Trans. Amer. Geophysical Union*, vol. 38, no. 6, pp. 913–920, 1957.
- [27] A. Wächter and L. T. Biegler, "On the implementation of an interior-point filter line-search algorithm for large-scale nonlinear programming," *Math. Program.*, vol. 106, no. 1, pp. 25–57, 2006.
- [28] P. R. Amestoy et al., "A fully asynchronous multifrontal solver using distributed dynamic scheduling," *SIAM J. Matrix Anal. Appl.*, vol. 23, no. 1, pp. 15–41, 2001.
- [29] L. A. Taber, "An optimization principle for vascular radius including the effects of smooth muscle tone," *Biophysical J.*, vol. 74, no. 1, pp. 109–114, 1998.
- [30] G. A. Salg et al., "Vascularization in bioartificial parenchymal tissue: Bioink and bioprinting strategies," *Int. J. Mol. Sci.*, vol. 23, no. 15, 2022, Art. no. 8589.